Synthetic model microswimmers near walls

Ketzetzi, S.

3

Diffusion-Based Analysis for Wall Distance Determination

Abstract

Microswimmers typically move near walls that can strongly influence their motion. However, direct experimental measurements of swimmer-wall separation remain elusive to date. In this chapter, we determine this separation for model catalytic microswimmers from the height dependence of the passive component of their mean-squared displacement. We find that swimmers exhibit "ypsotaxis", a tendency to assume a fixed height above the wall for a range of salt concentrations, swimmer surface charges, and swimmer sizes. Our findings indicate that ypsotaxis is activity-induced, posing restrictions on future modeling of their still debated propulsion mechanism.

The text in this chapter is based on:

S. Ketzetzi, J. de Graaf, D. J. Kraft, Phys. Rev. Lett. 125, 238001 (2020), "*Diffusion-Based Height Analysis Reveals Robust Microswimmer-Wall Separation*"; doi: 10.1103/PhysRevLett.125.238001

Introduction

Confining surfaces, such as planar walls, have a far-reaching impact in the microswimmer world, often ensuring microswimmer function and survival [18]. Encounters with surfaces give rise to accumulation, as seen for sperm [149], algae [150] and bacteria [151], and enable the formation of bacterial biofilms that facilitate their spreading, cooperation, and capture of nutrients [152–154]. Moreover, surfaces can significantly modify swimming trajectories; *e.g.*, bacteria often exhibit circular motion with direction controlled by the boundary condition [90–93], in stark contrast to their run-and-tumble motion in bulk.

Striking surface effects are not only found in biological systems, but are also present for synthetic microswimmers [59–61, 103, 105, 155, 156]. Model catalytic colloidal swimmers exhibit autonomous directed motion due to self-generated chemical gradients [83]. Recently, neighboring walls were shown to significantly alter the magnitude of their swim speeds [103, 105, 155, 156]. This revealed that walls play a far greater than previously expected role on self-propulsion, providing a path towards resolving seemingly conflicting experimental observations. For example, speed differences under similar conditions may stem from the phoretic interplay between the hydrodynamic boundary condition on the wall and the out-of-equilibrium chemical species generated by the swimmer [157]. Current models predict a wide range of behaviors close to walls, including hovering, sliding, forward and/or backward propulsion [58, 59, 95–102, 131–133, 158, 159]. This diversity is partly due to the complexity of and uncertainties in the propulsion mechanism, and partly due to the hydrodynamic and numerous phoretic couplings that wall proximity can introduce. Thus, quantitative insight into swimmer-wall separation is pivotal to pinpointing missing details of the propulsion mechanism, and in turn tailoring swimming behaviors, *e.g.*, for guiding microswimmers in complex environments.

To date, no reported experiment has directly measured swimmer-wall separations. However, based on qualitative observations, separations are anticipated to be smaller than the swimmer size [60, 75], even as small as a few tens of nm [113, 114]. Such separations cannot be directly resolved by standard optical microscopy [113], which is why holographic

microscopy has been proposed [105], as it yields three-dimensional positions of spherical particles with high precision [160]. However, fitting holograms of spheres half-coated with a metal is computationally expensive, especially when studying dynamics, since discrete dipole approximations have to be employed in the numerical calculations to obtain their positions [161]. Furthermore, inhomogeneities in the metal coating introduce additional fit parameters and uncertainties in determining particle positions. Another way to measure small particle-wall separations is Total Internal Reflection Microscopy, which yields separations from the scattering of evanescent waves off of particles close to a wall [162]. Here too, the asymmetric coating interferes with interpreting the result and obtaining accurate measurements. Hence, a novel measuring approach is needed.

In this chapter, we present a novel and straightforward method for obtaining microswimmer-wall separations *in situ*. We determine the translational diffusion coefficient of the swimmer from mean-squared displacement curves, and obtain the height from its theoretically predicted dependence on swimmer-wall separation. Our method can be applied to most synthetic microswimmers, and may be extended to a range of swimming microorganisms, moving parallel to walls. We applied it here to catalytically propelled model microswimmers. Besides the fuel concentration, we systematically varied additional parameters known to affect self-propulsion, as well as particle-wall separations in passive systems: the salt concentration in solution, swimmer size, and swimmer zeta potential. We were thereby able to gain unprecedented insights into their effect and the presence of a wall on the swimming behavior.

Results and Discussion

We obtained microswimmer-wall separations from experimental measurements of the separation-dependent translational diffusion coefficient, D, of the microswimmers. D as well as propulsion speeds V were extracted from mean square displacements (MSDs) following Ref. [30, 106]. Briefly, we fitted the short-time regime ($\Delta t \ll \tau_R$) of the MSDs with $\Delta r^2 = 4D\Delta t + V^2\Delta t^2$ [30]; τ_R is the rotational diffusion time, $\tau_R = 1/D_{R,bulk}$, with $D_{R,bulk} = \frac{k_B T}{8\pi\eta R^3}$ the bulk rotational diffusion coefficient, R the radius, η the viscosity, k_B the Boltzmann constant, and

T the absolute temperature. The first term corresponds to the passive diffusion contribution that is usually obscured by the activity-induced, short-time ballistic behavior [106], but may be obtained with sufficient statistics. Reliable measurements require frame-rate adjustment, such that the regime where both diffusion and activity contribute to the MSD can be resolved. See Methods for tracking and MSD calculation details.

To calculate the particle-wall separation, h, see also Figure 3.1, we first consider the ratio $d = D/D_{bulk}$, with $D_{bulk} = \frac{k_B T}{6\pi\eta R}$ the bulk diffusion constant. For $d \gtrsim 0.6$, the well-known prediction by Faxén [129, 130, 163, 164]: $d(h) = 1 - \frac{9}{16}\gamma + \frac{1}{8}\gamma^3 - \frac{45}{256}\gamma^4 - \frac{1}{16}\gamma^5$, with $\gamma = R/(h+R)$, can be used to extract h. For $d \lesssim 0.4$ a lubrication theory result, $d(h) = -\frac{1}{\frac{8}{15}\log\left(\frac{h}{R}\right) - 0.9588}$, is more appropriate [128, 165]. In the intermediate ($0.4 \lesssim d \lesssim 0.6$) regime, applicable to most of our experiments, we interpolate the combined numerical data by O'Neill [165] and Kezirian [123], see Methods for the $d(h)$ relation. Here, we fitted for h using the interpolated expression.

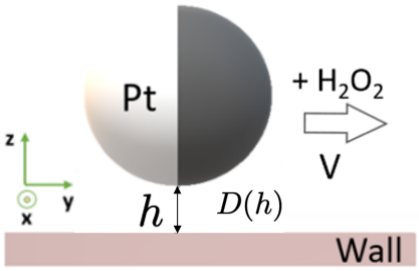

Figure 3.1: **Schematic of the experiment.** We obtain the swimmer-wall separation, h, from the measured translational diffusion coefficient, D, of the swimmer and its theoretically predicted dependence on wall separation.

In all experiments, we used monodisperse TPM colloids [108] half-coated with a thin Pt layer $\approx$ (4.5 $\pm$ 0.2) nm at dilute concentration. In water, colloids exhibited passive Brownian motion, while dispersion in 10% H_2O_2 rendered them active through a catalytic process. Colloids quickly reached the lower glass wall and continued to move adjacent to it, see Figure 3.1 for a schematic representation.

To demonstrate the effectiveness of our method, we first carried out control experiments in water. In these cases, D was acquired from fitting MSDs with $\Delta r^2 = 4D\Delta t$. Figure 3.2A shows that the extracted separation corresponds well to a theoretical prediction based on a balance of electrostatic repulsion and gravity [166, 167], see Appendix I. That is, we recovered the expected decrease in separation with increasing salt concentration: salt increases the solution's ionic strength, thereby effectively

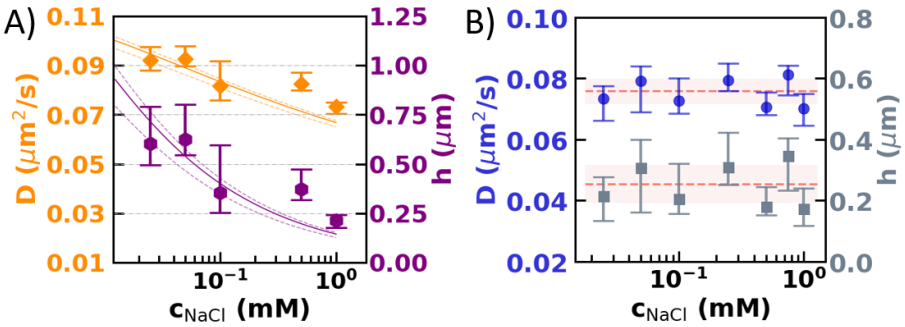

Figure 3.2: **Salt-dependent motion above the wall:** Effect of salt concentration c_{NaCl} on the motion of (2.77 ± 0.08) µm colloids with (4.4 ± 0.2) nm Pt. All reported values are medians, error bars denote first quartiles. A) Diffusion coefficient (orange) and separation (purple) in the Brownian state in water with c_{NaCl}. Lines show theoretical predictions based on balancing electrostatics and gravity, see Appendix I. B) Diffusion coefficient (blue) and separation (grey) in the active state in 10% H_2O_2 with c_{NaCl}. Dotted lines indicate mean values.

screening the charge on the particle and wall. This reduces the Debye length, *i.e.*, the distance over which surface charges act, bringing the colloids closer to the wall. To verify our method further, we compared separations resulting from our diffusion coefficient-based method to those directly measured with digital in-line holographic microscopy for uncoated silica spheres with well-known size and refractive index [168], see also chapter 5. The good agreement between the two methods confirms that we indeed recover colloid-wall separations with our diffusion-based method despite using a computed rather than a measured D_{bulk} value.

Having established the validity of our method, we employed it to our catalytic swimmers. First, we studied the effect of salt concentration in solution. For these experiments, we used TPM spheres of (2.77 ± 0.08) µm diameter half-coated with (4.4 ± 0.2) nm Pt. Surprisingly, in active systems we found a behavior completely unlike that of passive systems in Figure 3.2A. For the same particles and salt concentration range, D and h remain constant within measurement precision, see Figure 3.2B. Particles propel themselves parallel to the wall at constant separations of (0.25 ± 0.06) µm.

At the same time, we found a decrease in speed with increasing salt concentration, see Figure 3.3, where the line represents the least-squares fit with $V = A + (B/(C + c_{NaCl}))$. This expression follows from a salt-gradient based contribution to the observed speed [75], with A the remaining speed in the limit of high salt, B a prefactor, and C the ion concentration already present in the medium. From the fit we find (0.35 $\pm$ 0.09) µm/s and (0.09 $\pm$ 0.07) mM, for A and C, respectively. The fitted C value agrees reasonably well with the background ion concentration (0.008 mM) we obtained from electrical conductivity measurements [169] for 10% H_2O_2 (2.7 µS/cm, Ilium technology, Model 2100 Conductivity Meter) assuming hydrogen ions as the dominant ion species. We return to this salt gradient below.

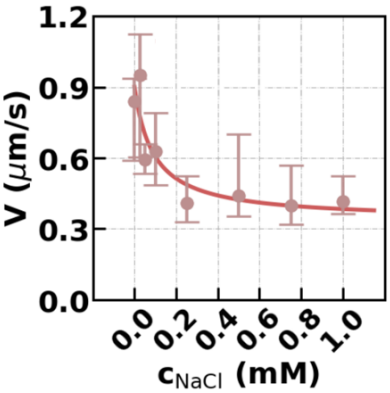

Figure 3.3: **Salt-dependent propulsion speed above the wall.** Speed decrease in 10% H_2O_2 with c_{NaCl}. Solid line is a least-squares fit with $V = A + (B/(C + c_{NaCl}))$, where A is the remaining speed in high salt, B a prefactor, and C the ion concentration already present in solution, following from ionic diffusioosmosis along the wall, see Appendix II.

Second, we explored the effect of colloid zeta potential, ζ, the electric potential at the colloid's surface. We used (2.70 $\pm$ 0.06) and (2.77 $\pm$ 0.08) μm diameter colloids with different surface functionalizations [136] and thus different ζ. The reported ζ correspond to those of the parent colloids, see Methods for characterization, before adding the Pt coating. We therefore use the adjective "base" and a subscript "b", *i.e*, ζ_b, to indicate that we know only the zeta potential of the uncoated colloid, and not that of the swimmer. We note that passive colloids with $\zeta_b > -12$ mV were typically stuck on the negatively charged wall, see also Methods (Figure 3.7B).

However, for the active system, we found that wall separation remained unaffected for the entire (wide) range of ζ_b under study, see Figure 3.4A. In all cases, particles moved at (0.24 $\pm$ 0.04) µm from the wall, which matches the separations measured for different salt concentrations. Unexpectedly, as we will return to, the colloids self-propelled not only at a constant h when varying ζ_b, but also at quantitatively comparable speeds

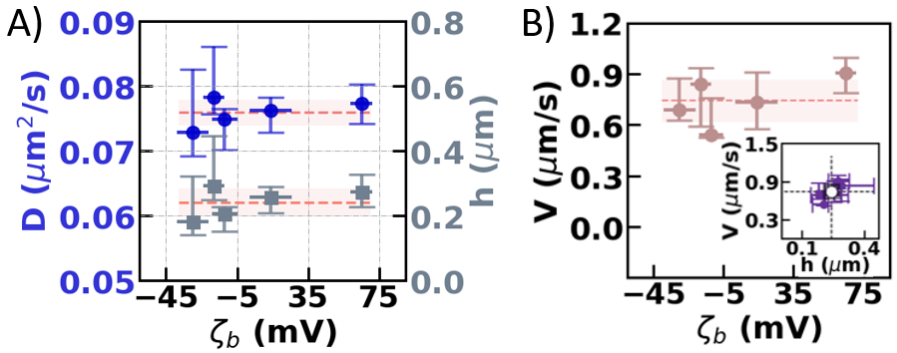

Figure 3.4: **Swimmer base zeta potential dependence of propulsion above the wall.** The base zeta potential, ζ_b, of TPM colloids with diameters between (2.70 $\pm$ 0.06) and (2.77 $\pm$ 0.08) µm, and Pt coating thicknesses $\approx$ (4.4 $\pm$ 0.2) nm, was varied through surface functionalization. All reported values are medians, error bars denote first quartiles, and dotted lines represent mean values. A) Diffusion coefficient (circles) and separation (squares) with ζ_b. B) Speed for the same ζ_b range as in (A). The inset shows propulsion speed with separation (purple circles), with the write circle marking the intersection of mean values.

V, see Figure 3.4B. We can indeed collapse the data by plotting V as a function of h, see the inset in Figure 3.4B, further demonstrating that ζ_b does not affect the swimming behavior. We note that the direction of motion was away from the Pt cap both for positive and negative ζ_b.

Third, we focused on swimmer size, another parameter known to affect swim speeds [58]. We performed experiments using TPM spheres with a wide range of radii, but with similar Pt coating thicknesses and ζ_b, see Methods. We found that diffusion coefficient decreases with swimmer size, see Figure 3.5A, where the solid line represents the least-squares fit with $D = a/R^b$ ($a = 0.120 \pm 0.004$ µm^3/s, $b = 1.3 \pm 0.2$). The inset shows the measured swim speeds together with a fit of the expected scaling $V = a/R$ [58] ($a = 2.2 \pm 0.4$ µm^2/s). Strikingly, swimmer-wall separation remained relatively constant with R, see Figure 3.5B; the dashed line shows the mean separation of (0.32 $\pm$ 0.08) µm.

The above experiments reveal that our swimmers exhibit "ypsotaxis": a tendency to assume a specific height for a wide range of parameters. Remarkably, the height appears independent of salt concentration, ζ_b,

and even size, running not only counter to our intuition for passive systems but also to features of common self-propulsion mechanisms. For our Pt-coated swimmers, this robust separation distance was found to be (0.27 $\pm$ 0.11) µm on average, in line with the observation that micron-sized catalytic swimmers do not self-propel over steps of a few hundred nanometers [60]. Such a height is further consistent with wall-dependent speeds [103, 105, 155, 156], for which wall separation must not substantially exceed the swimmer size to ensure strong osmotic coupling [59, 95, 100]. The wide range of swimmer sizes employed here showed that buoyancy is not the prime contributor to ypsotaxis. This is further underpinned by our observation of swimmers moving along the top wall, upon inversion of the sample holders, for a period of time. We hypothesize that ypsotaxis is instead primarily caused by phoretic and osmotic flows, *i.e.* it is activity-driven.

To test for this, we performed experiments using (2.23 $\pm$ 0.11) µm diameter TPM spheres with (4.5 $\pm$ 0.2) nm Pt for various H_2O_2 concentrations, and hence degrees of activity. Indeed, we found that diffusion coefficient and thus swimmer-wall separation not only decreases rapidly with increasing fuel concentration from the Brownian 0% H_2O_2 state (inset and

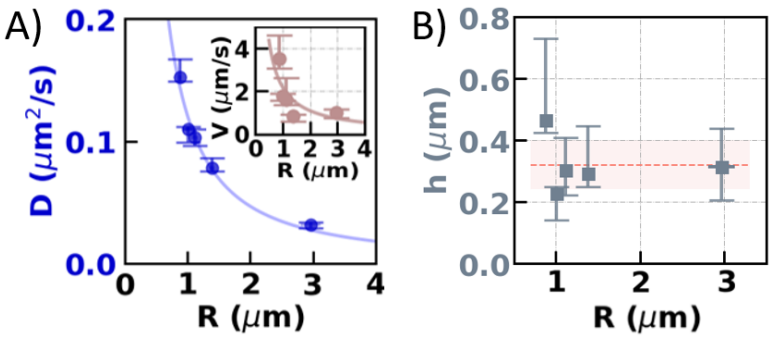

Figure 3.5: **Swimmer size-dependent propulsion above the wall.** All reported values are medians, error bars denote first quartiles. Variation of the radius, R, of active TPM spheres with similar ζ_b and Pt (coating thickness $\approx$ 4.5 $\pm$ 0.2 nm) affects A) the diffusion coefficient and B) swimmer-wall separation. The inset in (A) shows the propulsion speed with R. The solid lines in (A) are fits with a/R^b (main panel) and the expected a/R following from Ref. [58] (inset). The dotted line in (B) shows the mean separation (0.32 $\pm$ 0.08 μm).

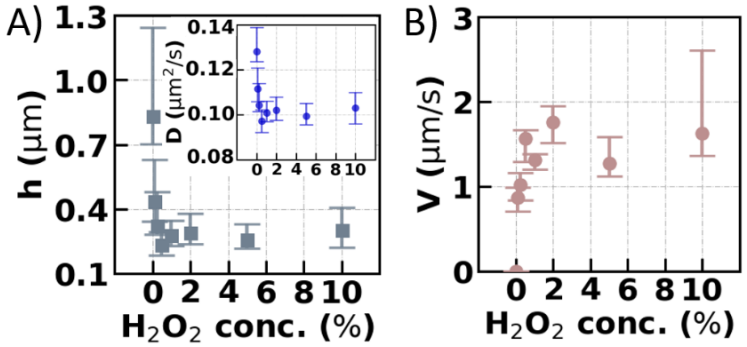

Figure 3.6: **Activity-induced ypsotaxis**. A) Swimmer-wall separation h with increasing H_2O_2 (fuel) concentration. The inset shows the corresponding diffusion coefficient D for the same concentration range. B) Speed V for the same fuel concentration range as in (A); the trend is similar to that of Refs. [30, 56]. Experiments were performed using (2.23 $\pm$ 0.11) μm diameter TPM spheres with (4.5 $\pm$ 0.2) nm Pt. All reported values are medians, error bars denote first quartiles.

main panel of Figure 3.6A, respectively), but also plateaus beyond 0.25% H_2O_2. Similarly, the speed also increases sharply and then plateaus above 0.25% H_2O_2 (Figure 3.6B). These observations imply that the constant separation is induced by the activity, thereby confirming our hypothesis on the origin of ypsotaxis. In Appendix III, we argue that said origin also causes the active alignment of catalytic swimmers with respect to the wall [59, 60, 81].

Our results provide new insights into the debated nature of the propulsion mechanism [76]. Current thinking favors self-electrophoresis [75, 89], *i.e.*, motion generated *via* self-generated ionic currents, as simple salts are known to greatly decrease propulsion speeds. The lack of speed variation with ζ_b, however, is not commensurate with this or other ion-based propulsion mechanisms typically scaling with ζ or ζ^2, see [74]. A possible explanation is that a different ζ at the Pt cap dominates the swimmer's behavior.

However, speed variation with salt — typically indicative of a change in activity — is not readily reconciled with a constant h which is also activity-driven, even if the cap's ζ dominates. Drawing upon our previous work [155], we provide an alternative wall-centric explanation. Suppose that the swimmer's bulk speed is unaffected by adding salt. The

swimmer's effective near-wall speed may still vary, provided salt impacts the osmotic counterflow induced by the swimmer-generated chemical species interacting with the wall [155]. Our fit in Figure 3.3 reveals that the osmotic contribution to the speed bears the hallmarks of ionic diffusion [63]. This requires a net-neutral gradient of ions with different electric mobilities to be involved, often referred to as a salt gradient. This salt gradient might originate from the chemical dissociation reactions in the long-range H_2O_2 gradient with the wall [74], stemming from fuel consumption at the Pt cap. This model would have the right features to show an ionic diffusioosmosis along the wall, see Appendix II for details.

Conclusions

In this chapter, we established a novel method for measuring swimmer-wall separations utilizing the height dependence of the diffusive component of their mean-squared displacement. We found that catalytic model microswimmers propel at roughly fixed heights of few hundred nanometers from planar walls. Our work further showed that nearby walls could be dominant factors in controlling swim speeds, *i.e.*, ion-induced flow may only play a role at the wall and not at the swimmer surface. This would necessitate a paradigm shift in modeling experimental observations and in identifying the still missing details of their propulsion mechanism. Our method can be readily applied to other types of spherical microswimmers moving parallel to walls, and may be extended to different swimmer shapes as well. We are confident that further application of our method will provide novel insights on the impact of confining surfaces in the microswimmer world and, in turn, facilitate predicting swimming behaviors in complex environments.

Acknowledgements

I am grateful to Joost de Graaf for his contributions to the development of the diffusion-based height analysis method, for developing the model of ionic diffusioosmosis and activity-induced ypsotaxis, and for many useful discussions. I thank Rachel Doherty for providing TPM colloids and for discussions on functionalizations. I also thank Ruben Verweij and Nikos Oikonomeas for discussions on holographic microscopy.

Methods

In this section, we provide additional details on particle preparation and characterization as well as describe the methods by which we obtained and processed MSD curves to subsequently infer the particle height.

Synthesis of bare TPM colloids. The bare TPM spheres used in Figures 3.2-3.6 were obtained from the one-pot surfactant-free synthesis protocol of Ref. [108]. In short, 30.0 g of a fresh stock solution of MilliQ water (18.2 MΩ cm resistivity, Filtration System Milli-Q Gradient A10) was weighed into a plastic beaker; the pH of the water was adjusted to 10.80 with ammonium hydroxide (28-30%, Sigma-Aldrich), and the solution was then stirred at 300 rpm. 900 µL TPM (98%, Sigma Aldrich) was rapidly injected into the water and the solution was covered with parafilm. After 20 min, the stirring speed was reduced and maintained at 200 rpm. After 2 h, 100 mg of azobis(isobutyronitrile) ($\geq$ 98%, Sigma-Aldrich) was added to the emulsion. The suspension was stirred a total of 2.5 h before heating in an oil bath at 80 °C under rotation of 50 rpm for another 2.5 h. The diameters of the colloid batches obtained with this protocol are found in Table 3.1. Different syntheses resulted in monodisperse spheres with diameters varying from 1.75 to 2.77 µm; size variation between syntheses is expected. The largest employed colloid batch was obtained through addition of the dye fluorescein isothiocyanate isomer I ($\geq$ 90%, Sigma-Aldrich) following Ref. [108]. Bare TPM particles are negatively charged in MilliQ water (pH 5.5), see also Table 3.1. In water at pH 3.3, the zeta potential increases indicating that the particles are less negatively charged than at pH 5.5.

Synthesis of carboxylated TPM colloids. Carboxylated TPM (TPM-COOH) spheres of diameter 2.70 $\pm$ 0.06 µm were prepared as in [155].

Amine functionalization of bare TPM colloids. Bare TPM spheres were modified with amine (NH_2) groups by silanization, resulting in positive colloid surface charges. Briefly, 14 mL ethanol (EtOH, Sigma-Aldrich), 3 mL NH_3 and 100 µL 3-aminopropyl triethoxysilane (APS, $\geq$ 98%, Sigma-Aldrich) were added in a glass vial and mixed at 300 rpm. 1 mL of 1% w/v TPM spheres in EtOH was subsequently added in the solution, which was then covered with parafilm. After stirring for 24 h, the particles were thoroughly washed in EtOH and subsequently in water.

NeutrAvidin-PEG-functionalization of carboxylated TPM colloids. The surface of the TPM-COOH spheres was functionalized with NeutrAvidin (Molecular Probes) and poly(ethylene) glycol (PEG), following the surfactant-free coating protocol established in Ref. [136]. Briefly, 13.8 mg EDC (1-Ethyl-3-(3-dimethylaminopropyl) carbodiimide hydrochloride, 99%, Carl Roth) and 4.6 mg NHS (N-Hydroxysulfosuccinimide sodium salt, 98%, Sigma-Aldrich) were dissolved in 1 mL water, previously kept at 4 °C. 250 µL of this solution was added in a 500 µL water solution containing 1% TPM-COOH spheres, previously kept at 4 °C; the solution was vortexed for 30 min at 4 °C. Subsequently, the pH was adjusted to 8.60 with 7.5 µL 0.2 M sodium hydroxide (NaOH, 98.5%, Acros Organics). 400 µL PEG (M_w = 2000, Alpha Aesar), taken from a 500 µL water solution containing 20 mg PEG, was added in the TPM-NHS particle solution. After vortexing for 48 h at 4 °C, the resulting PEG-coated particles (TPM-PEG) were thoroughly washed and stored in water. To check whether the PEG coating was successful, the TPM-PEG spheres were vortexed for 1 h in 2 M NaCl, after which aggregation was not observed. Moreover, we checked the bare zeta potentials (ζ_b) before and after PEG coating. In water, the original TPM-COOH spheres were measured to have $\zeta_b = -70 \pm 9$ mV while the TPM-PEG spheres had $\zeta_b = -40 \pm 7$ mV. This further indicated the presence of the PEG layer which shielded the COOH groups. The bare zeta potential decrease agrees with the one measured in Ref. [136] for 1 µm colloids after coating. The remaining negative surface charge is probably caused by unreacted COOH groups, as also mentioned by the authors of Ref. [136]. Note that in the acidic pH conditions of Figure 3.4 (pH 3.3), the bare zeta potential of the TPM-COOH spheres dramatically decreases to $\zeta_b = -12 \pm 7$ mV, which is expected since binding with hydrogen will neutralize the COOH groups. At the same time, the bare zeta potential of the TPM-PEG spheres is affected much less ($\zeta_b = -30 \pm 9$ mV) at pH 3.3.

Pt coating. All spheres were spin coated from ethanol dispersions on flat glass slides at sub-monolayer concentrations and subsequently sputter coated with Pt/Pd (80:20) from above, as described previously in the Methods of chapter 2. Thicknesses for all employed batches are shown in Table 3.1. These were determined electronically from the mass and the density of the deposited material using the Cressington Thickness Monitor, which measures thicknesses with resolution of order 0.2 nm. Note

that all particles have similar Pt thicknesses within error which ensures that any differences in observed behaviors do not arise from the thickness of the coating. After deposition the TPM/Pt colloids were redispersed in water (bare TPM and TPM-PEG spheres), or water containing 5 mM HCl (TPM-NH_2 spheres) or water containing 5 mM NaOH (TPM-COOH spheres) by sonication. Sonication typically took place for 10 to 20 minutes, during which time no Pt flakes were released from the glass slides in the solution. The colloids were subsequently washed and stored in water. Redispersion produced well-dispersed particles.

σ (µm)	PD (%)	surface groups	ζ_b (mV) pH 5.5
2.77 ± 0.08	2.8	-	-41 ± 9
2.70 ± 0.06	2.2	COOH	-70 ± 9
2.70 ± 0.06	2.2	PEG	-40 ± 7
2.77 ± 0.08	2.8	NH_2	—
2.77 ± 0.08	2.8	NH_2	—
1.75 ± 0.06	3.4	-	-44 ± 7
2.01 ± 0.06	3.0	-	-39 ± 7
2.23 ± 0.11	5.0	-	-44 ± 9
5.94 ± 0.31	5.2	-	-53 ± 10

σ (µm)	ζ_b (mV) pH 3.3	Pt ($\pm$ 0.2 nm)	Fig.
2.77 ± 0.08	-18 ± 6	4.4	3.2-3.5
2.70 ± 0.06	-12 ± 7	4.3	3.4
2.70 ± 0.06	-30 ± 9	4.3	3.4
2.77 ± 0.08	$+14 \pm 12$	4.3	3.4
2.77 ± 0.08	$+65 \pm 6$	4.4	3.4
1.75 ± 0.06	—	4.7	3.5
2.01 ± 0.06	—	4.5	3.5
2.23 ± 0.11	—	4.5	3.5-3.6
5.94 ± 0.31	—	4.5	3.5

Table 3.1: Overview of colloid properties for all batches employed in this chapter. Top from left to right, the columns provide: the diameter σ, the size polydispersity (PD) in percent, the groups (if any) present on the colloid surface after functionalization, the *bare* zeta potential ζ_b at pH 5.5. Bottom from left to right, the columns provide: the *bare* zeta potential ζ_b at pH 3.3, the thickness of the sputter-coated Pt layer, and the figure in which each colloid batch was used.

Colloid Zeta Potential Measurements. Measurements were performed at all times on the parent, i.e. uncoated, colloids using a Malvern Zetasizer Nano ZS, which measures the electrophoretic mobility of charged colloidal particles with laser doppler micro-electrophoresis. The colloid zeta potential is obtained from the electrophoretic mobility using Henry's equation [170] and the Smoluchowski approximation $\mu = \frac{\epsilon_r \epsilon_0}{\eta}\zeta$, incorporated in the Zetasizer's software. Typically, we performed 12-15 runs to obtain an accurate measurement of the zeta potential in water. Such measurements were then repeated two to five times for each batch. The results are reported in Table 3.1, showing that colloids of different sizes employed in Figure 3.5 have comparable zeta potentials. To determine potential differences in swimmer-wall separation and speed due to the swimmer zeta potential in Figure 3.4, we would have to determine the zeta potentials under conditions similar to the swimming experiments, *e.g.*, in H_2O_2. However, due to bubble formation at the electrodes of the cell measurements in H_2O_2 were not feasible. Since zeta potentials are set by the pH, the zeta potentials in Figure 3.4 were measured in water at pH 3.3 obtained by addition of HCl. This pH value is equivalent to that of the H_2O_2 solution.

Imaging and Tracking. In all swimming experiments, TPM/Pt colloids were dispersed in 10% aqueous H_2O_2 solution at dilute particle concentration ($\approx 10^{-7}$ v/v). Their motion was recorded above glass walls (glass cover slips, purchased from VWR and used as received) with a 60x oil objective (NA 1.4) mounted on an inverted Nikon Eclipse Ti microscope. 30 s movies were acquired in the xy-plane at a frame rate of 19 fps to allow access to short time scales. All measurements were performed in the dark to avoid photocatalytic decomposition of H_2O_2 and typically within the first hour after sample preparation to avoid depletion of H_2O_2 [75] and potential changes in substrate slip due to reaction with H_2O_2 [155]. Additional movies of the motion of TPM/Pt colloids were taken at 5 fps in water and water with pH 3.3, adjusted using HCl to match the pH of the swimming experiments in 10% H_2O_2. The duration of the control movies was adjusted with respect to the colloid size under study to ensure that motion was randomized: particles with diameter smaller than 2 µm were measured for 3 min, while particles with diameters between 2 and 3 µm were measured for 4 min, and particles with diameter 5.94 µm were measured for 6 min. Tracking was performed using Trackpy [141].

Fitting colloid-wall separations. In the Brownian (inactive) state, *i.e.*, in water without H_2O_2, the translational diffusion coefficient, D, of each TPM/Pt colloid was extracted by fitting individual MSD curves with $\Delta r^2 = 4D\Delta t$, where Δt is the lag-time. MSD calculation was performed using existing routines within Trackpy [141]. We typically fitted lag-times shorter than 2 s, for which we verified that the MSD data grew linearly in time; the power-law fit that we performed consistently yielded exponents of order 1 within these lag-times. For each distribution of D values, we extracted the median value and first quartiles. The reason for taking the median is to account for the asymmetry in the obtained distributions, primarily due to the presence of the wall; see Figure 3.7A for an example of the distribution of D values from 40 individual TPM/Pt colloids in water (colloid diameter 2.23 $\pm$ 0.11 µm). These measures gave the most satisfactory results in general in comparison with theory, see Figure 3.2A, to which we come back in Appendix I. We further checked in these control measurements that in-plane diffusion was random by additionally examining the MSDs in x and y directions separately. Extracting the corresponding diffusion coefficients revealed that these quantitatively agreed (values differ by less than 10%), confirming their random motion. We performed control experiments for colloids with different zeta potentials. As the zeta potential of the parent colloid ζ_b became more positive, the particles became irreversibly stuck on the glass wall, as expected. However, that

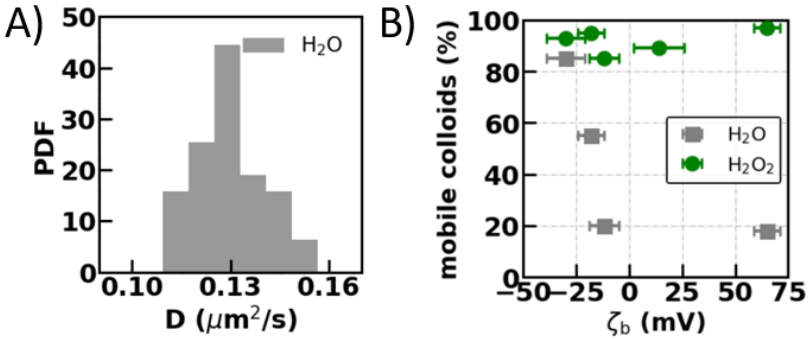

Figure 3.7: A) Distribution of translational diffusion coefficients D from 40 colloids (batch diameter 2.23 $\pm$ 0.11 µm) in the passive state in water. B) Fraction of mobile particles observed for colloids with a wide range of base zeta potentials ζ_b in the passive (H_2O, squares) and active (H_2O_2, circles) state at pH 3.3.

was not the case for the same particles in the active state. Figure 3.7B shows the fractions of mobile particles in the corresponding samples. For the experiments with positively charged parent colloids in their passive states, we still find a small percentage of mobile colloids. This is possibly due to the negatively charged Pt cap at pH 3.3.

In the active state, *i.e.*, in the H_2O_2 solution, D as well as the swim speed V were extracted from individual MSD curves using Eq. (2.3), the applicability of which we have already discussed in chapter 2. Returning to the fit expression given by Eq. (2.3), we are justified in using $D_{R,bulk}$ to evaluate τ_R, even close to a wall, since in-plane rotational motion is far less affected by the presence of a wall than out-of plane rotation, see Figs. 7 and 8 of Ref. [171]. Generally, rotation is influenced far less than translation, due to the more rapid decay of the associated hydrodynamic mode [128, 171]. In addition, Eq. (2.3) does not directly depend on τ_R. For each MSD curve, we performed a two parameter fit for D and V simultaneously. Figure 3.8A shows that if the passive component is omitted from the fit, the data is not fitted accurately with $V^2\Delta t^2$ alone (dashed line). However, the fit that does include the passive diffusion contribution $4D\Delta t$ follows the data perfectly (solid line). For the $\approx$ 2.7 µm diameter particles, MSDs were fitted up to lag-times of 0.4 s, as in chapter 2. For the 1.75 µm, 2.0 µm, 2.23 µm, and 5.94 µm diameter particles, MSDs were fitted up to lag-times of 0.22 s, 0.3 s, 0.35 s, and 0.6 s, respectively. The asymmetric nature of the V [155] and D distributions let us to extract and report median values in the Results and Discussion section. Asymmetry is expected when there are long-range, out-of-equilibrium interactions that couple to the wall. The wall distorts the flows and molecular gradients surrounding the swimmer, leading to an asymmetry in coupling between approaching and moving away from the wall, *i.e.*, this leads to an effective potential. Thus, asymmetry is an intrinsic property of our system, not a statistical one. Due to the skewed nature of the PDF, median values more accurately represent the average swim speed than means would. Figure 3.8B shows an example of such a distribution of D values obtained in the active state. Next, for each of our median values for D, we computed the reduced diffusion coefficient D/D_{bulk} using the bulk diffusion coefficient using $D_{bulk} = \frac{k_B T}{6\pi\eta R}$. This ratio, as we detail in the following section, corresponds to an established ratio of gap height h over particle radius R. We used the fitted value for D/D_{bulk} to extract the corre-

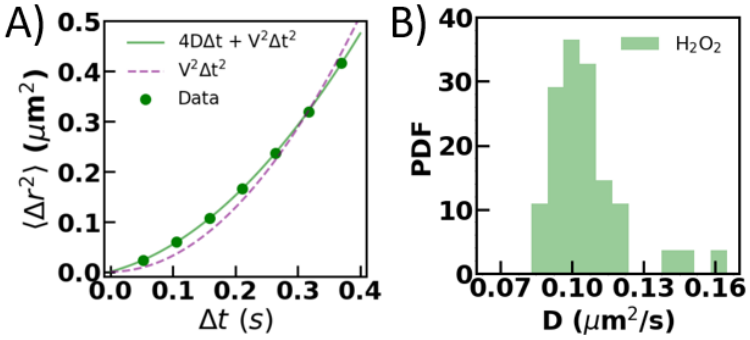

Figure 3.8: A) MSD curve for an individual colloid in the active state (data shown in green circles) fitted with $\Delta r^2 = 4D\Delta t + V^2\Delta t^2$ (green solid line) and $\Delta r^2 = V^2\Delta t^2$ (purple dashed line). B) Distribution of D coefficients from 40 colloids in the active state in H_2O_2 (colloid batch same as in Figure 3.7A), showing that the values are not normally distributed.

sponding h/R and associated first quartiles, see the following section for a discussion of the fitting. Lastly, we employed holographic microscopy to verify the accuracy of our approach. We measured the height distribution of Brownian 1 μm silica spheres with well-known refractive index in water [168] and found good agreement with the heights extracted following the here described diffusion-coefficient based method, as we detail in chapter 5, see also Figure 5.3 for a comparison to our prediction.

Height dependence of the diffusion coefficient. The Brownian motion of spherical particles immersed in a fluid near a plane wall has drawn the attention of the experimental community as a means to determine the gap height h between the particle and wall [129, 130]. This means of determining h relies on the hydrodynamic mobility, *i.e.*, the coupling between an applied force on the sphere and its observed speed, being substantially reduced by the presence of a wall [128]. Here, we briefly cover expressions found in the literature to approximate this reduction and how we combined these to fit for the height in our work. We will also indicate why activity and to a large extent wall wetting properties can be ignored.

The most commonly used expression for the effect of hydrodynamics on the mobility, or equivalently the gap-height-dependent diffusion $D(h)$ of a spherical particle above a *no-slip* wall ($\boldsymbol{u} = \mathbf{0}$ at the wall, with $\boldsymbol{u}$ the

fluid velocity) was derived by Faxén [163, 164] and reads

$$\frac{D(h)}{D_{bulk}} = 1 - \frac{9}{16}\gamma + \frac{1}{8}\gamma^3 - \frac{45}{256}\gamma^4 - \frac{1}{16}\gamma^5, \tag{3.1}$$

where $\gamma = R/(h+R)$ and the quadratic term drops out on the ground of symmetry. This expression was obtained using the method of reflections — applicable to the low-Reynolds-number regime that holds for our experiment, in which viscous dissipation dominates inertia. The limited number of reflections used in Faxén's derivation implies that expression (3.1) holds only for sphere-wall separations $h \gtrsim R$, see Figure 3.9A. For very small sphere-wall separations $h/R \ll 1$, results from lubrication theory apply as derived by Goldman, Cox, and Brenner [128]:

$$\frac{D(h)}{D_{bulk}} = -\frac{1}{\frac{8}{15}\log\left(\frac{h}{R}\right) - 0.9588}, \tag{3.2}$$

where the factor 0.9588 is a gauge that was applied to match the numerical data by O'Neill [165] in the near-field regime. Figure 3.9A shows the lubrication prediction and the O'Neill data. For completeness, we present additional numerical data obtained in the 1990s by Kezirian [123], which span the entire range, in the same figure. The $D(h)/D_{bulk}$ ratios obtained from our MSDs ($D(h)/D_{bulk} \approx 0.5$), mostly fell in the region between the respective ranges of applicability of the Faxén and lubrication expressions. From the comparison to the numerical data [123, 165] in Figure 3.9A, we notice that for $D(h)/D_{bulk} \lesssim 0.4$ Faxén's expression should not be trusted and the same holds for the lubrication expression for $D(h)/D_{bulk} \gtrsim 0.6$. In the overlapping range $0.4 \lesssim D(h)/D_{bulk} \lesssim 0.6$, both expressions give a 'reasonable' approximation of the ratio $D(h)/D_{bulk}$, *i.e.*, an accuracy of about 20% when establishing h is to be expected, with the former overestimating and the latter underestimating h. Analytic expressions that cover the range of interest to us do not exist, and for practical purposes it is cumbersome to perform the necessary numerical calculations for each obtained data point [123, 165]. We therefore complemented these expressions by a third-order interpolation to the log-log variant of the combined numerical data by O'Neill [165] and Kezirian [123]. This approach led to the black dashed curve shown in Figure 3.9A which can

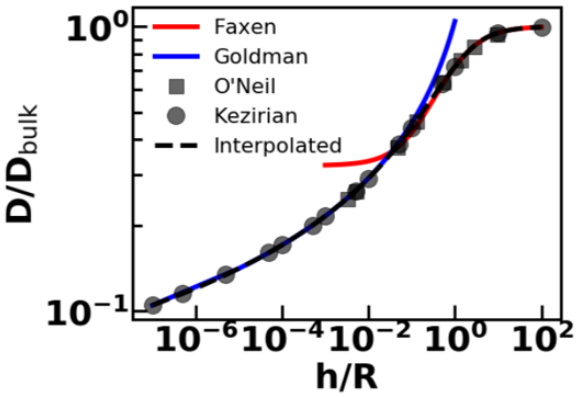

Figure 3.9: The change in the effective translational diffusion coefficient D — in terms of the bulk diffusion coefficient D_{bulk} — for a sphere with radius R as a function of the gap height h between the wall and the sphere surface. Log-log representation of various literature predictions and our own interpolated curve (dashed black) for a no-slip wall. The solid red curve corresponds to Faxén's prediction in Eq. (3.1) [163], the solid blue curve to the Goldmann, Cox, and Brenner result of Eq. (3.2) [128], the grey squares to the numerical results by O'Neill [165], while the grey circles to the numerical results of Kezirian [123].

generally be used to improve other experimental measurements of the height using our diffusion-based analysis approach. While our measured ratios fall inside the near-field regime of hydrodynamic interaction, where we need to resort to numerical results, this region fortuitously has significant sensitivity to variation in gap height, see Figure 3.9A. Thus, we were able to obtain accurate height measurements.

Appendix I: Balance between electrostatics and gravity in the passive system

Here, we introduce the Poisson-Boltzmann-based expressions and underlying assumptions for the salt-dependence of the height for a passive particle, which was used to determine the theory curves in Figure 3.2A. The solid and dotted orange curves in Figure 3.2A show the theoretical predictions that result from balancing electrostatics and gravity between colloids and wall in water. We make use of Poisson-Boltzmann expressions for the electrostatic repulsion rather than their linearized versions (Debye-Hückel). This is because the values of the zeta potentials of either surface are the least well-known quantities in our system. We consequently varied the zeta potentials over a reasonable range to estimate their effect, wherein we departed from the linear regime. Following, amongst others, Flicker and Bike [166] and Rashidi and Width [167] we arrive at the following force balance

$$\frac{4}{3}\pi\left(\rho_p-\rho_f\right)gR^3=\kappa B\exp\left(-\kappa h\right). \tag{3.3}$$

where the left-hand side represents the buoyant force, with the fluid mass density $\rho_f = 0.99\ 10^3$ kg m^{-3}, the TPM particle mass density $\rho_p = 1.314\ 10^3$ kg m^{-3} [108], the local gravitational acceleration $g = 9.81$ m s^{-2}, and the particle radius $R = 1.4$ µm. The right-hand side of Eq. (3.3) represents electrostatic repulsion [1] with

$$\kappa=\sqrt{\frac{2e^2C_{salt}}{\epsilon_0\epsilon_f k_BT}}, \tag{3.4}$$

$$B=64\pi\epsilon_0\epsilon_f R\left(\frac{k_BT}{e}\right)^2\tanh\left(\frac{e\zeta_{wall}}{k_BT}\right)\tanh\left(\frac{e\zeta_{part}}{k_BT}\right). \tag{3.5}$$

Equation (3.4) provides the inverse Debye screening length κ with e the elementary charge, $C_{salt} = C_{pH} + c_{NaCl}$ the salt concentration, which can be decomposed into a base conductivity contribution $C_{pH} = 3.16$ µM, the ion concentration calculated from the pH of the solution through $C_{pH} =$

[1] N.B. Flicker and Bike appear to use Gaussian units, as their B expression is missing a factor 4π with respect to Eq. (3.5).

$10^{(-pH)}$ for pH 5.5, and the amount of added sodium chloride c_{NaCl}, ϵ_0 the vacuum permittivity, $\epsilon_f = 80$ the relative dielectric constant of the fluid, k_B the Boltzmann constant, and $T = 300$ K the temperature. Equation (3.5) provides the electrostatic charge parameter, with ζ_{wall} and ζ_{part} the estimated zeta potential of the wall and particle, respectively. We took $\zeta_{wall} = \zeta_{part} = -50$ mV to compute the central solid line and $\zeta_{wall} = \zeta_{part} = -25$ mV and -75 mV for the lower and upper dashed lines in Figure 3.2A, respectively. By making these choices, there are no free parameters left and the equilibrium height may be extracted as a function of c_{NaCl}. Note that, given these reasonable zeta potential choices, the fit is excellent and appears to be mostly insensitive to the exact value of the zeta potential and more sensitive to the salt concentration. Examining the properties of the equation system further revealed that it is most sensitive to $(\rho_p - \rho_f)$; the fit may thus be improved by relaxing the constraint on ρ_p, though for this we are constrained by the literature [108].

Appendix II: Ionic diffusio-osmosis along the wall, rather than the swimmer

Here, we provide additional arguments in favor of ionic diffusioosmosis along a wall. There are various self-propulsion mechanisms that have been considered for Pt-coated Janus swimmers in H_2O_2, *e.g.*, see Ref. [74] for a brief overview. Most of the theory concerning mechanisms has focused on self-propulsion in bulk, ignoring the wall due to the symmetry break that it introduces, which hinders solving the associated Stokes-Poisson-Nernst-Planck equations in an analytic manner. There are, however, a large number of (numerical) studies of this more complicated geometry [95–97, 99–101, 158], but their focus is more often on the richness of behavior that simple models for self-propulsion can produce, by accounting for this symmetry break, rather than the propulsion mechanism. Turning to the experimental result, we observe that the lack of observed speed change when varying ζ_b in Figure 3.4B provides a potential clue that ionic effects are not dominating the dynamics of the swimmer itself. This is because both electrophoresis and ionic diffusiophoresis typically have linear proportionality in the zeta potential of the surface; the latter potentially even possessing a quadratic dependence on ζ_b [63]. In elec-

trophoresis, propulsion is a result of ions moving in a (self-induced) electric field coupling to a surface potential (or charge). Ionic diffusiophoresis is conceptually similar, but in this case the electric field is locally generated when there is a salt gradient in response to a difference in ion diffusion rates. Ionic diffusiophoresis can be the result of a Pt-based reaction that splits a neutral molecule into two charged species, *e.g.*, $H_2O_2 \rightarrow HO_2^-$ + H^+. Brown and co-authors have on separate occasions argued against neutral self-diffusiophoresis and ionic diffusiophoresis as viable candidates for self-propulsion *in bulk* [74, 75]. For both mechanisms, the numbers do not seem to be commensurate with the experimentally observed propulsion velocities. These calculations together with our observed lack of ζ_b-dependence of the swim speed leads us to conclude that other mechanisms may need to be considered to understand the motion of Pt-coated colloids. In modeling catalytic swimmers, the above observation could necessitate a return to a regular diffusiophoretic variant of H_2O_2 self-propulsion *in bulk* or a variation on the recently pitched 'rocket propulsion' [172] (presently it does not possess appropriate scaling with radius to describe our experiment) or even an, as of yet, unknown mechanism.

Nonetheless, there are clues that ions are important. Our experiments in which we vary the salt concentration showed a marked decrease of the observed swim velocity as a function of c_{NaCl}, in line with previous observations in the literature [75, 76]. We have shown in Figure 3.3 that our data is fitted well using the expression

$$V = A + \frac{B}{C + c_{\mathrm{NaCl}}}, \tag{3.6}$$

where V is the observed swim speed, and A, B, and C are fit constants, representing the remaining speed in the limit of high salt A, a concentration-to-speed conversion factor B, and the ion concentration already present in the medium C. Of the interfacial transport mechanisms described by Anderson [63], only the one based on ionic diffusion scales with $\kappa^{-2} \propto (C + c_{NaCl})^{-1}$. In addition, from our fit procedure we obtain the reasonable numbers 0.35 $\pm$ 0.09 µm/s, 0.05 µm mM/s, and 0.09 $\pm$ 0.07 mM, for A, B and C, respectively. In view of the above discussion, we thus interpret the fit in Eq. (3.6) as representing a term that governs bulk and non-ionic wall effects on

self-propulsion (A) and a term that describes an ionic diffusioosmosis along the wall (a combination of B and C). The latter generates a fluid flow along the wall, which acts on the swimmer and opposes its self-propulsion. The presence of a diffusioosmotic contribution implies that the reactions on the Pt surface must generate a salt gradient [74], *i.e.*, there must be a gradient of oppositely charged ionic species that differ in their electrophoretic mobility, though the exact nature of the involved ions remains speculative. This leads to an alternative interpretation of the swimming direction reversals through the addition of the ionic surfactant cetyltrimethylammonium bromide (CTAB) observed by Brown and Poon [75]. CTAB is known to affect the zeta potential and contact angle of surfaces. However, we have shown that changing ζ_b does not strongly impact the observed swim speed. We therefore argue in favor of a wall effect. That is, the reversal observed in Ref. [75] may be generated at the wall, through the adsorption of CTAB which impacts the induced osmotic flow. If there is indeed a sizeable effect of the wall, this sets a limit to the amount of bulk recombination of ionic species generated by the surface reactions [74] that can occur. That is, if ions are created at the surface of the swimmer, then they should not recombine before interacting with the wall. However, the recombination length was estimated to be 70 nm under typical experimental conditions [74], as is the case here; a length that is much smaller than the gap height. In addition, there is experimental evidence [173] that swimmers that move using ionic diffusion experience a limited near-wall effect on propulsion speed, though systematic variation of the wall zeta potential was not attempted in these systems. This speaks in favor of a relatively small recombination length, although the AgCl system in Ref. [173] is notably different from the H_2O_2-fueled swimmers employed by us.

The H_2O_2 gradient itself is, however, sufficiently long-ranged to bridge the gap between the swimmer and the wall. In addition, through dissociation reactions taking place in the bulk, involved in the association-dissociation equilibrium of $H_2O_2 \rightleftharpoons H^+ + HO_2^-$ [74], this H_2O_2 gradient leads to ionic gradients along the surface of the wall. This in turn can induce an ionic diffusioosmosis along the wall. However, it should be noted that generally the above reactions favor the associated state. Any ionic contribution resulting from dissociation is therefore weak compared to situations where H_2O_2 is forced to dissociate into its charged

constituents, which could take place on the Pt cap, as argued by Brown *et al.* [74]. These authors therefore disregarded dissociation of H_2O_2 as a viable self-propulsion mechanism for colloidal swimmers, since the associated gradients and consequently the speed are limited by the size of the swimmer. However, the gradient along the wall has a much larger surface to act over, which could lead to a more substantial contribution, even if the effect contributes little to self-propulsion itself. Lastly, while on the topic of speeds, we should comment on the inverse scaling of speed with size found for our swimmers, as previously reported by Ebbens *et al.* [58]. These authors made their observations away from walls, in the middle of the cuvettes they use. Therefore, the observed speed change in our system, when making an analogous change in radius, can most likely be attributed to the way the propulsion *in bulk* is influenced by the size of the swimmer, rather than due to an interaction with the wall. That is to say, the trend in the speed is not strongly influenced by aspects of the gap between the swimmer and wall, such as the local curvature. This speaks in favor of wall-based speed modification on scales larger than the gap height, *e.g.*, one governed by the gradient in H_2O_2. Note that it is unclear if the absolute value is modified with respect to the bulk speed based on our experimental data. Bulk measurements would be a next logical step in determining the full extent of the impact of the wall, possibly following the approach outlined in Ref. [173]. If a H_2O_2-gradient based ionic diffusioosmosis along the wall can be shown in this manner, more insight into the reaction specifics taking place at the Pt cap and the manner of self-propulsion may be gained.

Appendix III: Activity-induced ypsotaxis

Our experiments showed that TPM/Pt swimmers moving along a wall tend toward a constant height, a property that we refer to as ypsotaxis. This coincides with the speed of the swimmer plateauing when varying the H_2O_2 concentration, see Figure 3.6, strongly indicating that ypsotaxis is activity driven. At the same time, the chemical swimmers show a tendency to align their propulsion parallel to the wall [59, 81]. Das *et al.* [59] introduced a simple model for describing this orientational quenching, which we will now comment upon in relation to our work. Das *et al.* considered the contribution of several effects to orientational

quenching, including hydrodynamic interactions and electro- and diffusio-phoretic coupling. Estimating the relative contribution of each term, they concluded that a hydrodynamic coupling between swimmer and wall best explained their experimental observation, when the swimmer is propelled by a self-electrophoretic mechanism. However, combining our present results with our previous result on the effect of the contact angle of the nearby wall [155], we have shown that: (i) Phoretic flows along the wall can substantially influence the swimmer's dynamics. (ii) These flows are likely due to ionic diffusiophoresis. (iii) The mechanism of self-propulsion is probably not entirely commensurate with self-electrophoresis.

We found that h is roughly constant for the various sizes that we considered. This, however, does not mean that we expect this result to hold indefinitely. Very small swimmers have a tendency to reorient substantially and could (and have been observed) to move away from the wall more readily. Yet, surprisingly, a constant height approximation seems to capture the data well over the range of swimmer sizes for which we could conduct experiments. Over this range, the buoyant force changes by a factor of nearly 40, as the buoyant mass scales with R^3, not even factoring the weight of the larger (dense) Pt cap. It therefore seems unlikely that ypsotaxis is a result of a balance between gravity and an activity-related effect. Calculations on self-diffusiophoretic [58] and self-electrophoretic [74] swimming both predict a different scaling of swim speed with size that is not R^3, casting further doubt on such a balance. The subdominance of buoyancy was further underpinned by experiments showing that the self-propelled particles can, for a time, move along the top surface of an inverted sample cell. Here, gravitational contributions are pointing in the opposite direction with respect to the surface normal, yet the phoretic/osmotic contributions maintain their orientation with respect to the surface. Nonetheless, we should point out that previous experiments support a greater separation between less dense swimmers and the wall [61, 75]. That is, their swimmers have $D \approx D_{bulk}$, while our TPM swimmers (a substantially denser material) attain $D \approx 0.5D_{bulk}$, which speaks for a limited gravitational effect, but clearly not a dominant one. Das *et al.* argued that their orientational quenching was a consequence of the activity only. Based on our Figure 3.6 we can extend this conclusion

to ypsotaxis and we can even go further and suggest a common origin. It is, at present, unclear how activity would lead to a constant self-propulsion height with the observed variation of self-propulsion speed, as we have undercut the self-electrophoretic argument by Das *et al.* for this mechanism. We leave the exact way in which this happens open to future investigation, as without further experimental evidence in favor of a specific self-propulsion mechanism there remain too many free parameters to solve the problem. Nonetheless, our experimental evidence in favor of a constant height is strong and should serve to bound future modeling.